

# <sup>1</sup> Chapter 1

## <sup>2</sup> Experimental results

### <sup>3</sup> *Diamond irradiation study*

<sup>4</sup> This chapter contains the measurement results of data taken with diamond sensors.  
<sup>5</sup> The description of measurement setup (section 1.1) is followed by applying experi-  
<sup>6</sup> mental techniques and a discussion of results in order to find operational limitations  
<sup>7</sup> in sections 1.2.1, 1.4 and 1.5. The aim of the chapter is to compare the experimentally  
<sup>8</sup> acquired data with the theory from the previous chapter and to define limitations of  
<sup>9</sup> the diamond detectors in terms of noise, radiation and temperature.

<sup>10</sup> Diamond sensors are mainly used for two types of measurements: particle counting  
<sup>11</sup> and spectroscopy. The first type of measurements depends on the sensor's efficiency  
<sup>12</sup> – the ability to detect all or at least a known percentage of particles/photons that  
<sup>13</sup> hit it. The energy of the radiation is not so important; what bears the information  
<sup>14</sup> is the rate and the spatial distribution. Here the radiation does not necessarily stop  
<sup>15</sup> in the bulk, but rather continues its way. In spectroscopy, on the other hand, the  
<sup>16</sup> idea is that a particle stops within the sensor, depositing all its energy, which is then  
<sup>17</sup> measured via the freed charge carriers. The aim of the experiments described in this  
<sup>18</sup> chapter is to:

- <sup>19</sup> 1. Quantify the efficiency of the sCVD diamond in counting mode,
- <sup>20</sup> 2. Quantify the degradation of efficiency with respect to the received radiation  
dose,
- <sup>22</sup> 3. Quantify the macroscopic effects on charge carrier behaviour with respect to  
the received radiation dose and
- <sup>24</sup> 4. Define limitations for its use in spectroscopy.

<sup>25</sup> The results discussed here show that there are several limitations for using dia-  
<sup>26</sup> mond as a measurement device. All of them need to be taken into account for the  
<sup>27</sup> measurement device to perform reliably and stably. The first step is to build a setup  
<sup>28</sup> that is insensitive to environmental interferences and minimises electrical noise in  
<sup>29</sup> the system. The setup needs to be calibrated before use. Then, the measurement

## 1.1. MEASUREMENT SETUP

---

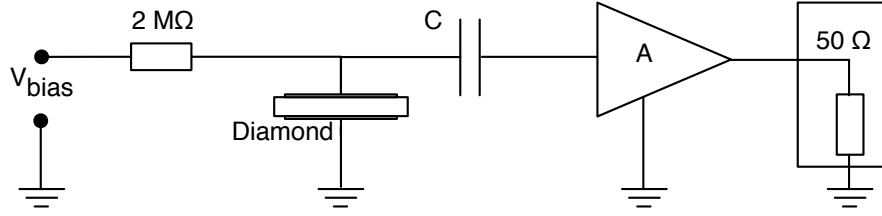


Figure 1.1: Diagram of a diamond detector readout chain.

30 conditions have to be defined, such as the temperature, the type of radiation and its  
31 flux. This allows us to estimate the lifetime of the detector and predict the longterm  
32 change of the signal. This change can then be accounted for when interpreting the  
33 output data.

### 34 1.1 Measurement setup

35 As said in the introduction, in order to get reliable measurement results, great care  
36 has to go towards designing a measurement setup that minimises the noise in the  
37 measurements. Shielding has to be applied wherever possible. For instance, alu-  
38 minium foil can be wrapped around the exposed parts of the system to shield them  
39 from external radio-frequency (RF) interferences. In addition, the sensors have to be  
40 covered to prevent the light from shining directly onto them.

41 The measurements using diamond that are explained in these chapters were carried  
42 out using several measurement setups, but they are all similar in terms of the electrical  
43 signal chain. The measurement chain consists of three main parts: a diamond sensor,  
44 a signal preamplifier and a readout device, as seen in diagram 1.1. The signals  
45 propagating along the analogue chain (before being digitised by the readout device)  
46 are fast – in the GHz bandwidth range – and with low amplitudes, which gives rise  
47 to importance of RF shielding. Also, the connection between the carrier and the  
48 preamplifier has to be as short as possible to avoid capacitive signal losses in the  
49 transmission line. Finally, the system needs to be grounded properly.

#### 50 1.1.1 Preamplifiers

51 Two preamplifiers were used for the measurements, one sensitive to charge and the  
52 other to current. *CIVIDEC Cx* (figure 1.2a) is a charge shaping amplifier. Its high  
53 SNR (low noise of 400 electrons and a reported gain of  $\sim 8.2$  mV/fC) makes it a  
54 good choice for spectroscopic measurements with diamond sensors. *CIVIDEC C2*  
55 (figure 1.2b) is a fast current preamplifier with a 2 GHz bandwidth limit. It is  
56 used for TCT measurements because of its fast response and a good SNR. Both are  
57 embedded in an RF-tight aluminium box to reduce the noise pickup. Both have an  
58 AC coupled input and a  $50 \Omega$  output.

## 1.1. MEASUREMENT SETUP

---

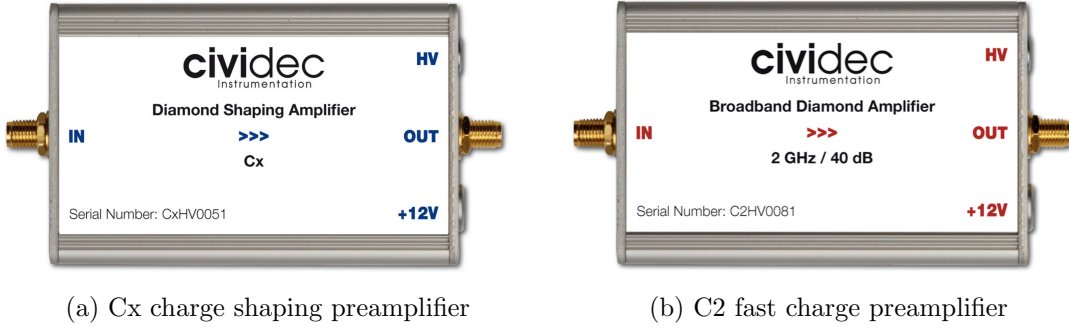


Figure 1.2: Amplifiers used for the charge and current measurements

### 59 Calibration

60 The amplifiers were calibrated before use to determine their gain. Both were cal-  
 61 ibrated using a square signal generator with a known amplitude step of  $U_{in} =$   
 62  $(252 \pm 5)$  mV. A 2 GHz oscilloscope with a 10 GS/s sampling was used to carry  
 63 out these measurements.

64 In the case of the Cx charge sensitive amplifier, the signal was routed through a  
 65 capacitor with a calibration capacitance  $C_{cal} = (0.717 \pm 0.014)$  pF and then to the  
 66 input of the amplifier. The pulse area behind the capacitor was  $a_{cal} = 5.0 \pm 0.5$  pVs  
 67 and the signal amplitude on the output was  $U_{amp} = (1.95 \pm 0.05)$  V. The input  
 68 voltage step combined with the calibration capacitance yields a calibration charge  
 69  $Q_{cal} = C_{cal} \cdot U_{in} = (181 \pm 5)$  fC. The gain of the Cx amplifier is therefore  $A_{Cx}^Q =$   
 70  $\frac{U_{Cx} Q_{cal}}{a_{cal}} = (9.3 \pm 0.4)$  mV/fC or  $A_{Cx}^a = \frac{U_{Cx}}{a_{cal}} = (390 \pm 40)$  mV/pVs. The area-based  
 71 amplification factor has a higher uncertainty ( $\sim 10\%$ ) than the amplitude-based  
 72 factor ( $\sim 4\%$ ) due to the measurement limitations of the oscilloscope. Nevertheless,  
 73 it can be used as an estimate for the integrated charge of a current pulse.

74 To calibrate the C2 current amplifier, only the amplitude gain had to be measured.  
 75 The input signal amplitude had to be such that it kept the output amplitude within  
 76 the amplifier's linear range, that is  $\pm 1$  V. The signal from the generator was therefore  
 77 routed through a 36 dB attenuator to decrease its amplitude to  $U_{inAtt} = (3.95 \pm$   
 78  $0.05)$  mV. Two amplifiers with different gains were measured, because both were  
 79 used for the measurements at different times. The output of the first amplifier was  
 80  $U_{C2-1} = (860 \pm 5)$  mV. This yields the amplification gain equal to  $A_{C2-1} = \frac{U_{inAtt}}{U_{C2-1}} =$   
 81  $(217 \pm 3)$ . The second amplifier had the output equal to  $U_{C2-2} = (632 \pm 5)$  mV with  
 82 the gain equal to  $A_{C2-2} = (152 \pm 3)$ .

### 83 1.1.2 Diamond samples

84 The diamond detector business is a niche market, with only a handful of producers  
 85 existing worldwide. Detector-grade diamonds are very difficult to produce, mostly  
 86 because it is very difficult to ensure a high enough purity of the lattice. It takes  
 87 companies years of trials to produce high enough quality product. Since the target

## 1.1. MEASUREMENT SETUP

---

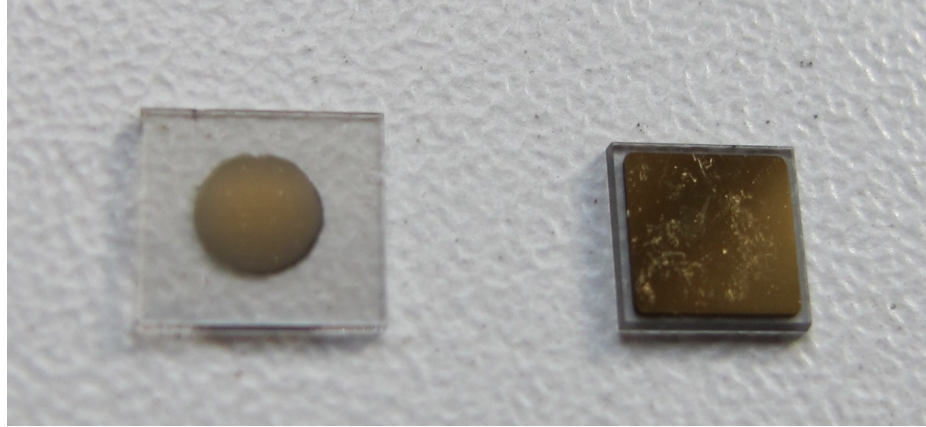


Figure 1.3: Two scCVD diamond samples: A IIa 1scdhq (left) and an E6 S37 (right)

market are almost exclusively particle physics research institutes, the companies work closely with them to make sure the product is up to par with the requirements. All sensor samples used to carry out these studies were bought at Element Six (E6). They all have the same dimensions, which have become a kind of standard. sCVD diamonds with dimensions  $4.7 \times 4.7 \text{ mm}^2$  are already sufficiently large for most of the beam monitoring applications and still affordable; the price for sCVD diamonds grows exponentially with the area. There is also an ongoing race among the producers to produce larger and larger diamonds while maintaining the price tag. For instance, a rather young player in this field, IIa from Singapore, has produced high-quality samples with larger dimensions and the diamond detector community is currently involved in extensive tests of their products. One of the samples with dimensions of  $5.6 \times 5.3 \text{ mm}^2$  was also sent to the PH-ADE-ID group at CERN to be characterised. The target thickness for all the samples is  $500 \mu\text{m}$ . Diamonds this thick yield a high enough signal-to-noise ratio for MIPs to be measured by the electronics. Table 1.1 shows all the samples used for this study. Two of them were later irradiated with  $300 \text{ MeV}$  pions and then compared to the pre-irradiated state. Irradiation doses for damaging the material need to be high – above  $10^{12}$  particles per  $\text{cm}^2$  to be able to observe change in the sensor’s behaviour.

Name	Type	Producer	Dimensions (x, y) [mm <sup>2</sup> ]	Thickness [μm]	Irradiated
S37	sCVD	E6	$4.7 \times 4.7$	548	no
S50	sCVD	E6	$4.7 \times 4.7$	537	no
S52	sCVD	E6	$4.7 \times 4.7$	515	$1 \times 10^{14} \text{ p/cm}^{-2}$
S79	sCVD	E6	$4.7 \times 4.7$	529	$3.63 \times 10^{14} \text{ p/cm}^{-2}$
ELSC	sCVD	E6	$4.7 \times 4.7$	491	no
1scdhq	sCVD	IIa	$5.6 \times 5.3$	460	no

Table 1.1: Diamond sensor samples used

The diamond samples have quoted impurity densities of  $\leq 2 \times 10^{14} \text{ cm}^{-3}$  and nitrogen incorporation of  $\leq 1 \text{ ppb}$ . The electrodes were added by various companies

## 1.1. MEASUREMENT SETUP

---

and institutes. For instance, S52 was metallised by DDL while the Physics Department of the University of Firenze, Italy metallised the S79. There are also several techniques for producing the electrodes. The DDL contacts consist of three layers: DLC (diamond-like carbon)/Pt/Au with 4/10/200 nm thicknesses, respectively. The metallisation for S79, on the other hand is made up of Cr/Au with a total thickness of  $\sim 400$  nm. The area coverage also differs from sample to sample. Diamonds must not be metallised until the very edge as the proximity of contacts with a high potential can lead to sparking. However, since only the areas not covered by the metallisation are sensitive, this effectively reduces the sensitive area of the sensors. In the diamonds used here the effective area was anywhere from  $9\text{ mm}^2$  to  $18\text{ mm}^2$ . Leakage current through the bulk was below 1 ns, but increased for the irradiated samples. The capacitance was of the order of  $(2.0 \pm 0.3)$  pF.

### 1.1.3 Readout devices

Electrical signals in diamond detectors are in the GHz frequency range. To preserve this information, the readout device has to have a high bandwidth limit. For instance, a 250 MHz limit is enough for the spectroscopic measurements with the Cx charge amplifier, but might be insufficient for the current measurements with the C2 amplifier. Two devices were used take data shown in this chapter. The first choice was a 2 GHz LeCroy WaveRunner 204MXi-A. This specific model has a high enough limit for the fast current preamplifier signals. It offers a versatile solution for analogue signal readout – it is fast to set up and reliable. It is very convenient for use in lab tests and for experiments where small amounts of data are taken and where speed is not crucial. However, its slow acquisition speed turned out to be a bottleneck in the test beam experiment. Its initial 100 Hz readout rate decreased to a mere 20 Hz within 20 minutes, because every single trigger was saved as a separate file and the Windows operating system was not capable of handling 10000+ files in a single directory easily. This is why it was exchanged with a DRS4, an analogue readout device developed by PSI, Switzerland. This compact device is capable of recording up to four waveforms at a time at a steady rate of up to 500 Hz. Its 700 MHz bandwidth limitation was sufficient for the signal from the charge amplifier.

### 1.1.4 Setup for the efficiency study using $\beta$ particles

The efficiency study of the diamond sensors was carried out at CERN in a test beam facility called the North Hall. There a straight high-energy particle beam of 120 GeV pions (marked  $\pi$ ) was provided to the users to calibrate their detectors. The size of the beam was approximately  $\sigma = 10$  mm and the particle rate was of the order of  $10^4 \pi \text{ cm}^{-2} \text{ s}^{-1}$ . A diamond sensor embedded in a PCB carrier was placed in the beam spot perpendicular to the beam. It was connected via an SMA connector directly to a charge amplifier (described below). The amplified signal was read out using a LeCroy oscilloscope and a DRS4 analogue readout system (both described below). A computer was used as a controller and data storage for the readout device.

## 1.1. MEASUREMENT SETUP

---

150 A separate system was used as a reference detector. It is called the *beam telescope* and  
151 is a device used to cross-check the measurements of the devices under test (DUTs) and  
152 to carry out spatially resolved studies on the DUTs. It consists of several pixellated  
153 sensor planes placed in series, which can track a particle's trajectory with a precision  
154 of a few microns. The sensor planes are positioned in front of the DUT and behind  
155 it. Then the beam telescope acts as a trigger system – it triggers the readout of  
156 both the telescope data and DUT data when both the planes in front and behind the  
157 DUT recorded a hit by the impinging particle. A particle detected by all the planes  
158 within the DUT window and the DUT itself counts towards its efficiency whereas a  
159 hit missed by the DUT counts against it. To discard the hits missing the DUT, a  
160 region of interest (ROI) can be chosen in the beam telescope planes.

### 161 1.1.5 $\alpha$ -TCT setup

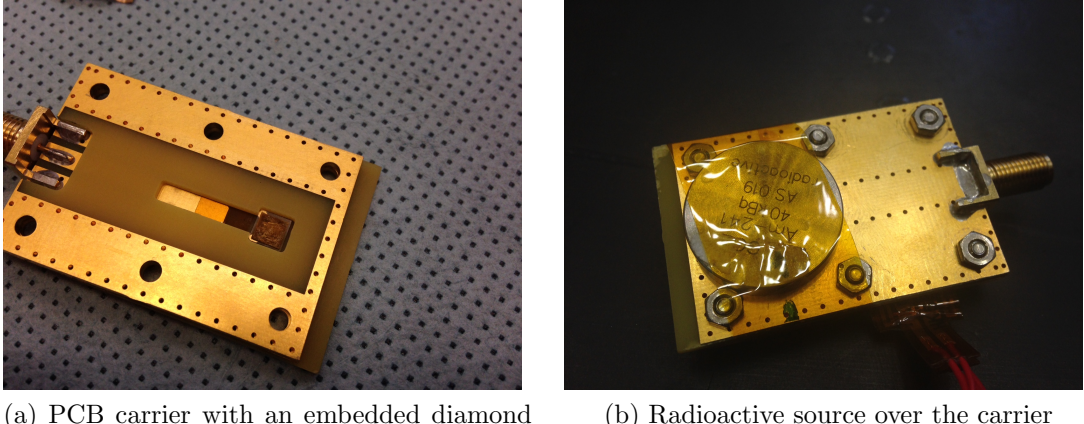
162 Room-temperature TCT measurements were carried out in the lab. The setup con-  
163 sisted of a diamond sensor embedded in a PCB carrier, a current amplifier and an  
164 oscilloscope. To measure  $\alpha$  particles, their energy loss during their trajectory had  
165 to be minimised. Therefore the diamond was placed inside a vacuum chamber. The  
166 chamber was a steel tube with a diameter of 5 cm. On one side it was connected to a  
167 vacuum pump via an steel pipe. A feedthrough with an SMA connector was placed on  
168 the other side. A C2 current amplifier was connected directly onto the feedthrough.  
169 The amplified output was connected to the oscilloscope via an SMA cable. An  $^{241}\text{Am}$   
170 source with a diameter of 2 cm and a height of 0.5 cm was placed onto the sensor  
171 carrier (figure 1.4a) and fixed in place using kapton tape (figure 1.4b). Then the  
172 carrier was inserted in the chamber and fixed in place using an air-tight clamp. The  
173 pump was then switched on. It was capable of providing the inside pressure as low  
174 as  $10^{-4}$  mbar after approximately one hour of operation, but measurements could  
175 take place even after five minutes of evacuation, at around  $10^{-3}$  mbar. The most  
176 important thing to bear in mind was to switch the bias voltage of the sensor OFF  
177 during the process of evacuation, because the air becomes more conductive at the  
178 pressure of the order of  $10^{-1}$  mbar. A failure to switch off the bias voltage would  
179 cause a spark between the signal and ground line, destroying the amplifier. Yes, this  
180 did happen in the course of carrying out these measurements.

### 181 1.1.6 Cryogenic $\alpha$ -TCT setup

182 The experiment at cryogenic temperatures was carried out in the cryolab at CERN.  
183 The room-temperature TCT setup had to be modified to allow for measurements at  
184 temperatures as low as 2 K. It consisted of three parts: 1) a cryostat – a thermally  
185 insulated cylinder capable of containing liquid helium, 2) an inlet – an air-tight me-  
186 chanical tube with valves and feedthroughs at the top that is lowered in the liquid  
187 helium and 3) the diamond sample, a temperature sensor, a heater and cables leading  
188 to the feedthroughs.

## 1.1. MEASUREMENT SETUP

---



(a) PCB carrier with an embedded diamond sample      (b) Radioactive source over the carrier

Figure 1.4: Positioning of the  $\alpha$ -source on top of the sensor carrier

When the diamond sample was placed in the PCB carrier and the  $^{241}\text{Am}$  source was in place, the inlet was sealed and lowered in the empty cryostat. Then the inside volume of the inlet was evacuated to down to  $10^{-5}$  mbar while the liquid helium was flowing into the cryostat. To improve the thermal contact between the diamond and the outside of the inlet, a small amount of helium gas was added inside the evacuated inlet, setting the vacuum to around  $10^{-3}$  mbar. This value changed with time, because the gas condensed on the walls of the inlet, reducing the number of floating particles. For this reason the helium gas had to be added from time. This caused a significant undershoot of the sample temperature, which had to be corrected for with the heater. Also, the added gas deteriorated the vacuum inside the inlet. It was very important to monitor the pressure so as not to let it rise above  $10^{-2}$  mbar. The air at this pressure is significantly more conductive and could cause a short circuit between the two diamond plates or in the SMA connectors, destroying the amplifier. Actually, it once did. Furthermore, at approximately 60 K the helium gas had to be evacuated from the inlet to avoid a potential explosion due to the expansion of the gas with temperature. Anyway, when the sample was cooled to the minimum temperature achievable by use of liquid helium without over-pressurising it (4.2 K), the measurements started. After every temperature data point, the current through the heater placed in the PCB next to the diamond sample was increased, warming up the sample. The initial temperature time constant of the order of tenths of seconds at low temperatures increased with temperature and even more so when helium was evacuated from the inlet at 60 K, removing the thermal bridge between the wall of the inlet and the diamond sample. At RT, the time constant was already of the order of minutes.

**213 1.2 Particle and photon pulses and spectra**

214 In previous chapter the ionisation profiles for different types of radiation were dis-  
215 cussed. It is known that  $\beta$  particles and  $\gamma$  radiation both create a triangular pulse  
216 whereas  $\alpha$  particles create a rectangular one. However, their amplitude, width and  
217 rise/fall time depend heavily on the type of interaction with the diamond, the purity  
218 of the diamond and the bandwidth of the amplifier and the oscilloscope. This section  
219 shows the signal pulses of  $\alpha$ ,  $\beta$  and  $\gamma$  radiation with their respective energy distribu-  
220 tions for the case of a diamond detector. Then follows a discussion of effects of noise  
221 on these measurements.

222 A CIVIDEC C2 current amplifier together with the LeCroy oscilloscope (both  
223 with a bandwidth limit of 2 GHz) was used to record the pulse shapes whereas the  
224 Cx charge amplifier was used for area distribution measurement. A 2 GHz bandwidth  
225 limit defines the minimum rising time equal to  $t_r \simeq \frac{0.34}{BW} = \frac{0.34}{2 \times 10^9} = 170$  ps, therefore  
226 the system is capable of measuring pulses with a minimum FWHM  $\simeq 170$  ps. This  
227 already makes impossible to measure the initial peak in  $\alpha$  response due to the two  
228 flavours of charge carriers travelling. If the flavour travelling through the bulk takes  
229  $t_{t1} \sim 6$  ns to get to the electrode on the other side ( $d_1 \sim 500$   $\mu m$ ), the other with  
230 a shorter path to the closer electrode – max.  $d_2 \sim 10$   $\mu m$  – already recombines in  
231  $t_{t2} \sim \frac{d_2}{d_1} t_{t1} = 120$  ps. This is too fast for the C2 amplifier or the oscilloscope to be  
232 able to observe.

233 Figure 1.5 shows a set of pulses and an averaged pulse for  $\alpha$ ,  $\beta$  and  $\gamma$  radiation as  
234 measured by the non-irradiated sCVD diamond S37.  $\alpha$  particles always produce the  
235 same signal pulse, with a high noise RMS. The averaging suppresses the noise while  
236 still retaining most the information. It does, however, smear the rising and falling  
237 edge, increasing the rise time. The  $t_r$  is now of the order of 0.5 ns. Both  $\beta$  and  $\gamma$   
238 pulses look similar - triangular and with a wide range of amplitudes. Here the pulse  
239 count is low, so the really high pulses were not recorded, because they are very rare.  
240 A trigger set very high would be needed to “catch” them with the oscilloscope.

**241 1.2.1 Noise limitations**

242 Noise is a major limiting factor in particle detection. It defines the minimum measur-  
243 able particle energy and the minimum measurement resolution. It is hence important  
244 to minimise the electric noise in the detector signal. The major noise contribution  
245 comes from poor shielding from external electromagnetic sources. These often cause  
246 ringing, whereby the signal oscillates with a frequency defined by the external source.  
247 The ringing makes high-frequency measurements impossible. Another source of noise  
248 is the sensor itself. In the case of silicon, natural light increases the number of ther-  
249 mally excited free charge carriers, increasing the leakage current. This is not the  
250 case for diamond, which is with its high energy band gap insensitive to visible light.  
251 Nevertheless, any noise produced by the sensors is amplified by the signal ampli-  
252 fiers, which add an additional noise of the analogue electrical circuit to the amplified  
253 signal. Finally, the digitisers add the quantisation noise to the digitised signal. If

### 1.3. RADIATION LIMITATIONS

---

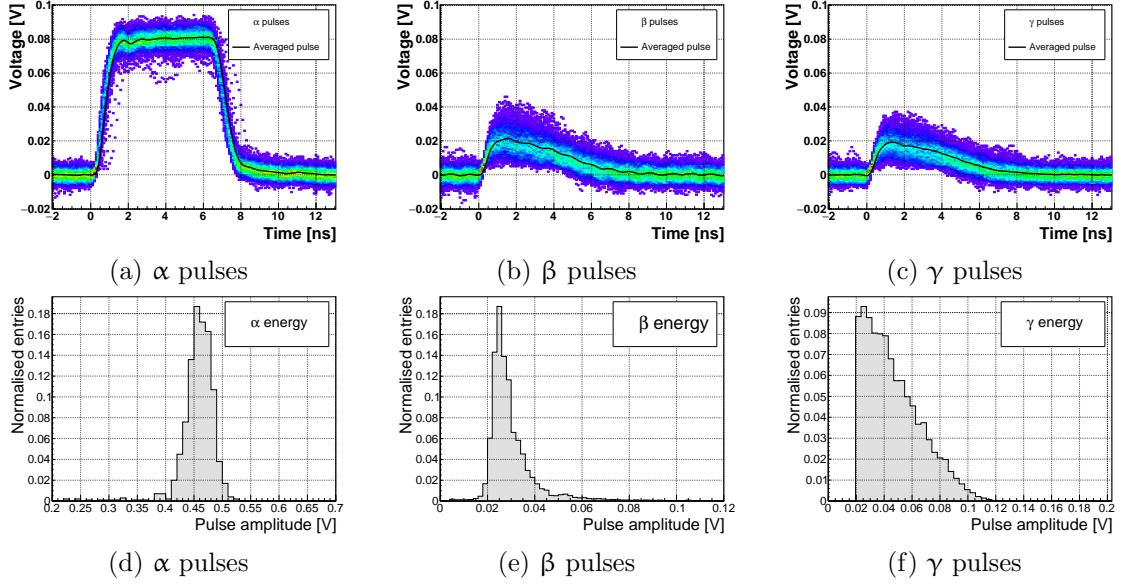


Figure 1.5: Superimposed and averaged pulses (a, b and c, current amplifier) and distributions of deposited energy (d, e, f, charge amplifier) for three types of radiation. Mind the scale on the X axis of the distributions.

254 the measurement range is significantly higher than the actual measured signal, the  
 255 quantisation noise can be a significant contributor to the decrease of the overall mea-  
 256 surement resolution.

## 257 1.3 Radiation limitations

258 Exposure to ionising radiation degrades sensors. It introduces charge traps by dam-  
 259 aging the sensor material. The electrons and holes created by the impinging particle  
 260 get trapped in these traps, decreasing the induced current on the electrodes. This  
 261 yields a lower integrated charge in an irradiated sensor than that in a non-irradiated  
 262 one. Charge collection efficiency is therefore correlated with the level of irradiation.  
 263 This section tries to study the effects of pion ( $\pi_{300 \text{ MeV}}$ ) irradiation on the efficiency  
 264 of sCVD diamond detectors. To carry out this study, two diamond samples were irra-  
 265 diated to  $1 \times 10^{14} \pi \text{ cm}^{-2}$  and S79 to  $3.63 \times 10^{14} \pi \text{ cm}^{-2}$ . Then a test beam campaign  
 266 was carried out to observe the charge collection efficiency at different bias voltage  
 267 settings. The highest achieved efficiency values were used to determine the effective  
 268 drop in efficiency with respect to received radiation dose. A model defined by a col-  
 269 laboration researching diamond behaviour called RD42 was applied to the measured  
 270 values and a damage factor was extracted. The factor agreed quite well with the re-  
 271 sults obtained by the RD42. The next subsection contains measurements and results  
 272 of a long-term stability study using  $\alpha$  and  $\beta$  particles. It is shown that the charge  
 273 collection efficiency of the irradiated samples improves in time for  $\beta$  radiation, but  
 274 deteriorates severely for  $\alpha$  radiation. To investigate this effect on the scale of charge

### 1.3. RADIATION LIMITATIONS

---

275 carriers, the change of TCT pulses with time is observed. Finally, a procedure that  
276 improves the pulse shape and with it the charge collection is proposed.

#### 277 1.3.1 Quantifying radiation damage in diamonds

278 The last few decades have seen extensive efforts put into understanding and quanti-  
279 tifying radiation damage in semiconductors. This varies with the type of radiation  
280 (particles or photons) and its energy. There are models existing that try to explain  
281 the impact of irradiation and to provide *hardness factors* to compare the radiation  
282 damage between different particles. The standard way is to convert the damage into  
283 *neutron equivalent*. Some models have been extensively verified with simulations and  
284 experimentally. In these experiments charge collection in sensors is measured before  
285 and after irradiation. This procedure is repeated several times, with a measurement  
286 point taken after every irradiation. When a set of measurements of charge collection  
287 is plotted against the radiation dose received by a specific particle at a specific energy,  
288 a damage factor  $k_\lambda$  can be extracted. Damage factors have to be measured across a  
289 range of energies and types of particles (photons) to properly quantify the damage  
290 in the sensors. They are then compared against the simulations to verify that the  
291 experimental observations are in line with the theory.

292 Radiation damage in silicon, for instance, is well understood and explained. Sili-  
293 con sensor is relatively cheap and widespread, which facilitates the irradiation exper-  
294 iments. Diamond, on the other hand, is an expensive material and the technology  
295 is relatively new as compared to silicon. Therefore not many institutes are carrying  
296 out diamond irradiation studies. To join the efforts, a collaboration called RD42 was  
297 formed. It gathers the experimental data from diamond irradiation studies. Unlike  
298 with silicon, the experimental results so far show no significant correlation with the  
299 NIEL (non-ionising energy loss) model [?], which correlates detector efficiency with  
300 the *number of lattice displacements*. Therefore an alternative model was proposed  
301 by Karlsruhe Institute of Technology [?], correlating the diamond efficiency with *dis-*  
302 *placements per atom* (DPA) in the bulk. Figure 1.6 shows the DPA model for a range  
303 of energies of proton, pion and neutron irradiation in diamond. According to the plot,  
304 a 300 MeV pion beam damages the diamond bulk twice as much as a 24 GeV proton  
305 beam. The data points obtained by RD42 are also added to the plot. They have been  
306 normalised to damage by 24 GeV protons. In the end, the data point measured in  
307 the scope of this thesis was added for comparison.

#### 308 Pion irradiation

309 Paul Scherrer Institute (PSI) is the largest research institute for material sciences in  
310 Switzerland. Among other tasks they also carry out irradiation campaigns. They  
311 use a beam of 300 MeV/c pions  $\pi$  (kinetic energy 191.31 MeV) with a flux of up to  
312  $1.5 \times 10^{14} \pi \text{ cm}^{-2} \text{ day}^{-1}$ . The machine has a 10 % uncertainty on the beam energy. In  
313 addition, due to the uncertainty on the hardness factor, the equivalent fluencies have  
314 an error of  $\pm 20 \%$ . Looking at figure 1.6,  $\pi_{300 \text{ MeV}}$  sit on a steep section of the DPA

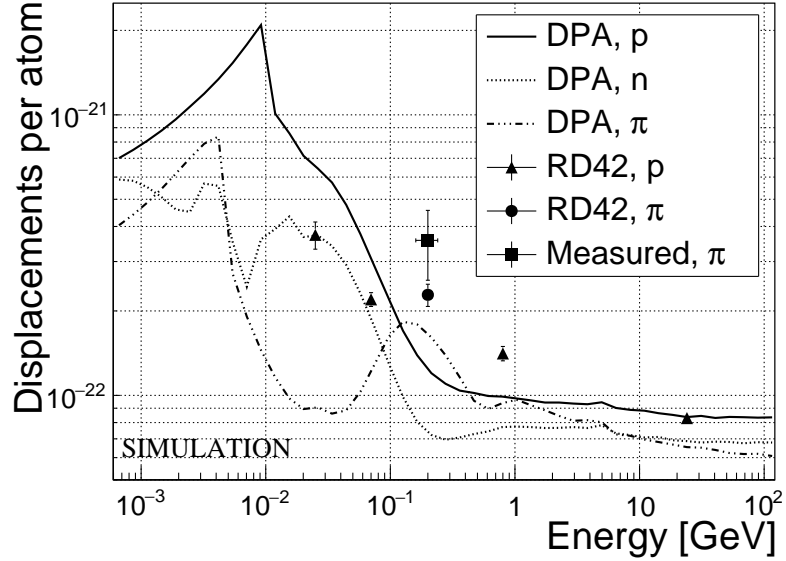


Figure 1.6: Diamond radiation damage - a model based on displacements per atom [1]. Added are data points for protons and pions by RD42 and one data point for pions measured in the scope of this thesis.

315 distribution. After fitting a linear function to this part of the distribution, the error  
 316 on the DPA due to the uncertainty on the beam energy amounts to 7 %. Overall  
 317 error on the fluency is therefore the root mean square of the uncertainty on the DPA  
 318 and the uncertainty on the hardness factor:  $\sigma = 21 \%$ .

319 Two diamond samples, S52 and S79, were exposed to the pion beam in the 2014  
 320 PSI irradiation campaign; S52 to  $(1 \pm 0.21) \times 10^{14} \pi \text{ cm}^{-2}$  and S79 to  $(3.63 \pm 0.77) \times$   
 321  $10^{14} \pi \text{ cm}^{-2}$ . During the process, the golden electrodes got slightly activated, but the  
 322 activation decayed in two weeks.

### 323 Charge collection distance

324 Three diamonds – non-irradiated S37 and irradiated S52 and S79 – were exposed to a  
 325 120 GeV test beam before and after irradiation to estimate the charge collection dis-  
 326 tance (CCD) and its decrease after irradiation. The samples were primed (“pumped”)  
 327 prior to data taking using a  $^{90}\text{Sr}$  radioactive source. Data were then taken at a range  
 328 of bias voltages from 30 V to 500 V, yielding up to  $1 \text{ V}/\mu\text{m}$  electrical field in the bulk.  
 329 Every data point contained approximately  $5 \times 10^4$  measured particles. The charge  
 330 deposited by the particles was measured using a CIVIDEC Cx charge preamplifier.  
 331 As expected, the integrated amplitude spectrum followed a landau distribution. Its  
 332 most probable value (MPV) was used to calculate the most probable collected charge  
 333  $Q_i$ :

$$Q_i [e] = Q_i [fC] \cdot 6.241 \times 10^{18} = \frac{\text{MPV} [\text{mV}]}{A [\text{mV}/fC]} \cdot 6.241 \times 10^{18} \quad (1.1)$$

### 1.3. RADIATION LIMITATIONS

---

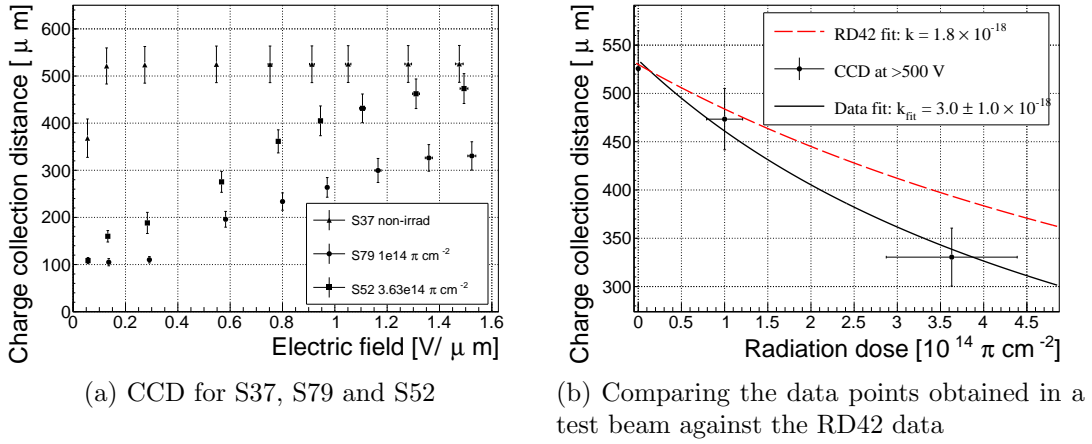


Figure 1.7: The charge collection distance at 500 V bias voltage for the three diamond samples was compared to the RD42 data for pion irradiation. The data points are for about 5–15 % lower than expected from the RD42 data.

334 where  $A = 9.2 \text{ mV/fC}$  is the preamplifier gain factor. The CCD was then calculated  
 335 using the average number of electron-hole pairs produced per micrometer in diamond  
 336  $\delta_d = 36 \text{ e-h } \mu\text{m}^{-1}$ :

$$CCD = \frac{Q_i}{\delta_d} \quad (1.2)$$

337 The resulting CCD for the three measured samples at bias voltages ranging from  
 338  $0.2\text{--}1.6 \text{ V } \mu\text{m}^{-1}$  is shown in figure 1.7a. S37 exhibits full collection distance already  
 339 at  $0.4 \text{ V } \mu\text{m}^{-1}$  whereas the irradiated samples have a more gentle increase of CCD  
 340 with increasing bias voltage. It is evident that at  $1 \text{ V } \mu\text{m}^{-1}$  the maximum CCD has  
 341 not been reached in the case of S79 and S52.

#### 342 Irradiation damage factor

343 The irradiation damage factor  $k$  is a way to quantify irradiation damage of a specific  
 344 particle at a specific energy. Via this factor different types of irradiation can be  
 345 compared. It is obtained experimentally by measuring the CCD of a number of  
 346 samples at various irradiation steps and fitting the equation 1.4 to the data.  $\lambda$  is the  
 347 measured CCD,  $\lambda_0$  is the CCD of a non-irradiated sample and  $\Phi$  the radiation dose.

$$\frac{1}{\lambda} = \frac{1}{\lambda_0} + k_\lambda \cdot \Phi \quad (1.3)$$

$$\lambda = \frac{\lambda_0}{k_\lambda \lambda_0 \Phi + 1} \quad (1.4)$$

349 The data points with the maximum CCD obtained in the test beam measurements  
 350 were plotted against radiation dose received (see figure 1.7b). Equation 1.4 was fitted  
 351 to the data points and a damage factor  $k_\lambda = (3.0 \pm 1.0) \times 10^{-18} \text{ } \mu\text{m}^{-1} \text{ cm}^{-2}$  was  
 352 obtained. This value is for a factor of two higher than the damage factor obtained by

### 1.3. RADIATION LIMITATIONS

---

353 RD42. A possible cause is that the irradiated samples did not yet have a full charge  
354 collection at  $1.5 \text{ V } \mu\text{m}^{-1}$ . Also, with only two samples measured, the statistical  
355 uncertainty was high. Nevertheless, it can be concluded that the 300 MeV pions  
356 damage the diamond bulk more than the 24 GeV protons.

#### 357 1.3.2 Long-term measurement stability

358 An important requirement for particle detectors is stable performance over long pe-  
359 riods of time. For instance, the charge collection for a defined type and quantity  
360 of radiation must not change over time or has to change in a predicted way. Dia-  
361 monds are arguably stable, as long as their environment and operating point does  
362 not change. The stability of diamond detectors depends on many external factors.  
363 The aim is to study the behaviour of diamond under controlled conditions, with the  
364 goal to understand its limitations. One of these limitations is for sure the received  
365 radiation dose. It might affect the long-term stability of the sensor during operation.

366 The three diamond samples (S37, S79 and S52) were exposed to two different types  
367 of ionising radiation for a longer period to see if their behaviour changes over time.  
368 Two parameters were observed in particular: 1) charge collection of  $\beta$  particles and  
369 2) charge collection and ionisation profile of  $\alpha$  particles. The results showed in both  
370 cases that *priming* plays an important role in diamond measurement stability. The  
371  $\beta$  particles have a healing effect on the diamond; MIP detection is therefore rather  
372 stable in the long run, despite the degradation due to irradiation. Alpha particles,  
373 on the other hand, deteriorate the measurement by introducing space charge into the  
374 sensor bulk.

#### 375 $\beta$ measurements

376 The samples were intentionally not primed before the measurements took place. The  
377 same initial conditions are usually found in HEP experiments. The measurement  
378 setup consisted of a diamond sample with the Cx spectroscopic amplifier, a silicon  
379 diode with a C6 amplifier for a trigger and a  $^{90}\text{Sr}$  source on top. A particle emitted by  
380 the source traversed the sensor bulk and hit the silicon diode, triggering the analogue  
381 signal readout. The source was left on the top for the course of the experiment. The  
382 measurements, however, took place at discrete times. For every data point, approx-  
383 imately  $10^4$  triggers were recorded. The offline analysis of the recorded signal pulse  
384 amplitudes yielded a landau distribution for every data point. The resulting graph of  
385 charge collection over time showed that the charge collection efficiency improves over  
386 time. This is especially evident in the case of the two irradiated samples. S79 achieves  
387 close to full efficiency whereas S52 reaches about 75 %. Both increases are significant.  
388 After some time the signal stabilises. As expected, the signal of the non-irradiated  
389 S37 did not change with time – this pure sCVD diamond sample had the maximum  
390 collection efficiency from the start.

391 It should be noted that the  $\sim 2.28$  MeV electrons emitted by this source are not  
392 MIPs, because they sit far to the left on the Bethe-Bloch function and therefore

### 1.3. RADIATION LIMITATIONS

---

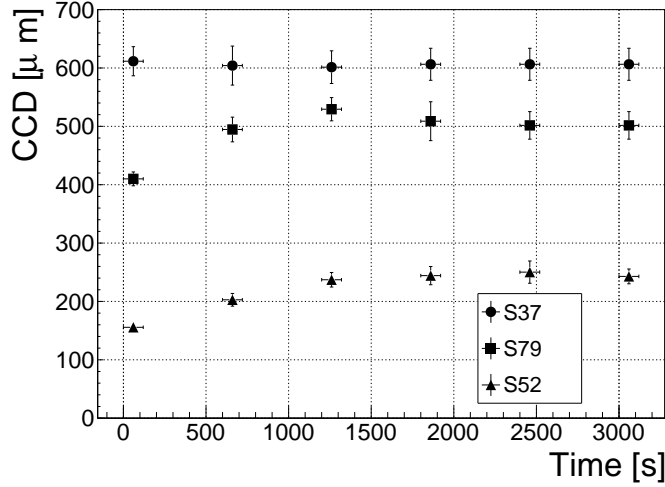


Figure 1.8: Increase of charge collection over time due to priming with the  $^{90}\text{Sr}$  radioactive source

393 deposit more charge in the bulk than the regular MIPs. Nevertheless, for the purpose  
394 of these measurements this energy was adequate since only the relative change in  
395 charge collection was of our interest.

396 To sum up, diamond is an adequate material for use in  $\beta$  radiation detection.  
397 Even if damaged by radiation, it reaches equilibrium in the order of an hour and  
398 exhibits stable charge collection from then on. The efficiency decreases with received  
399 radiation dose, but the decrease can be accounted for if the damage factor and the rate  
400 energy of the particles are known.  $\gamma$  radiation has a similar impact on the diamond  
401 as the  $\beta$ . The impinging photons, if they interact with the diamond, prime the bulk,  
402 causing the increase in charge collection efficiency. The difference, however, is in the  
403 interaction probability (cross section), which is several orders of magnitude lower for  
404 gammas.

#### 405 $\alpha$ measurements

406 This part discusses the stability of irradiated diamond sensors during  $\alpha$  measure-  
407 ments. It is justified to assume that they will behave differently than when subject  
408 to  $\beta$  radiation. This is due to the point-like charge carrier creation when an  $\alpha$  par-  
409 ticle impinges the bulk. The energy is approximately 20 times higher than the most  
410 probable value of a MIP; deposited in a small volume, it will behave differently to the  
411 track-like energy deposition of MIPs. In addition, carriers of only one polarity drift  
412 through the sensor while the others almost instantly recombine with the adjacent  
413 electrode. Taking into account that the diamond bulk has been damaged by irradia-  
414 tion, these two phenomena might have an effect on the operation of the detector on  
415 a macro scale.

416 The measurement setup consisted of a PCB carrier for a diamond with a fitted

### 1.3. RADIATION LIMITATIONS

---

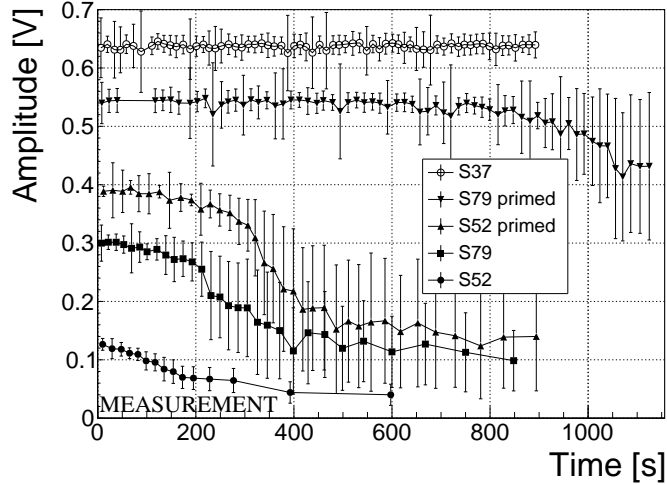


Figure 1.9: Comparison of collected charge with time for non-irradiated and irradiated diamond samples.

<sup>417</sup> <sup>241</sup>Am source and a vacuum chamber. The carrier was placed into the chamber, which  
<sup>418</sup> was evacuated. It acted as shielding for external noise pickup and ensured that the  
<sup>419</sup>  $\alpha$  particles didn't lose energy traveling through air. An SMA feedthrough ensured  
<sup>420</sup> the electrical connection to the outside. The samples were measured before and after  
<sup>421</sup> priming, at both polarities, to compare the behaviour of both electrons and holes as  
<sup>422</sup> charge carriers. The scope of the measurements was to observe the eventual changes  
<sup>423</sup> in charge collection efficiency and/or in the pulse shapes.

<sup>424</sup> The first test was carried out using the Cx spectroscopic amplifier. The bias  
<sup>425</sup> voltage of the samples was set to +500 V and the signals from the diamond were  
<sup>426</sup> measured for  $\sim$ 15 minutes. Figure 1.9 shows the results of these measurements. The  
<sup>427</sup> collected charge for the non-irradiated sample was stable with time. It was expected  
<sup>428</sup> that the irradiated samples will have a lower charge collection efficiency than their  
<sup>429</sup> non-irradiated counterpart. However, their initial efficiency suddenly dropped after  
<sup>430</sup> a certain period of time. Priming did improve their efficiency, but it only deferred its  
<sup>431</sup> eventual drop. In addition, the spread of measured energies increased significantly.  
<sup>432</sup> Also, the particle counting rate decreased with the decreased efficiency.

<sup>433</sup> The next step was to observe the behaviour of the current pulse shapes with time  
<sup>434</sup> using a C2 current amplifier. The shape of the pulse holds more information about the  
<sup>435</sup> micro-processes in the sensor than solely the value of the integrated charge. This time  
<sup>436</sup> only the primed sensors were tested. Both hole and electron collection were observed  
<sup>437</sup> to determine whether they behave differently or not. The samples were measured long  
<sup>438</sup> enough for the pulse shapes to start changing. The data in figures 1.10 show that the  
<sup>439</sup> pulses start changing in a chaotic way – suddenly there are several different shapes,  
<sup>440</sup> some still the same as at the beginning while the others with almost zero amplitude.  
<sup>441</sup> These data are difficult to interpret. Nevertheless, the idea is that some charges get  
<sup>442</sup> trapped in the charge traps in the bulk for a long time, building up regions of space

### 1.3. RADIATION LIMITATIONS

---

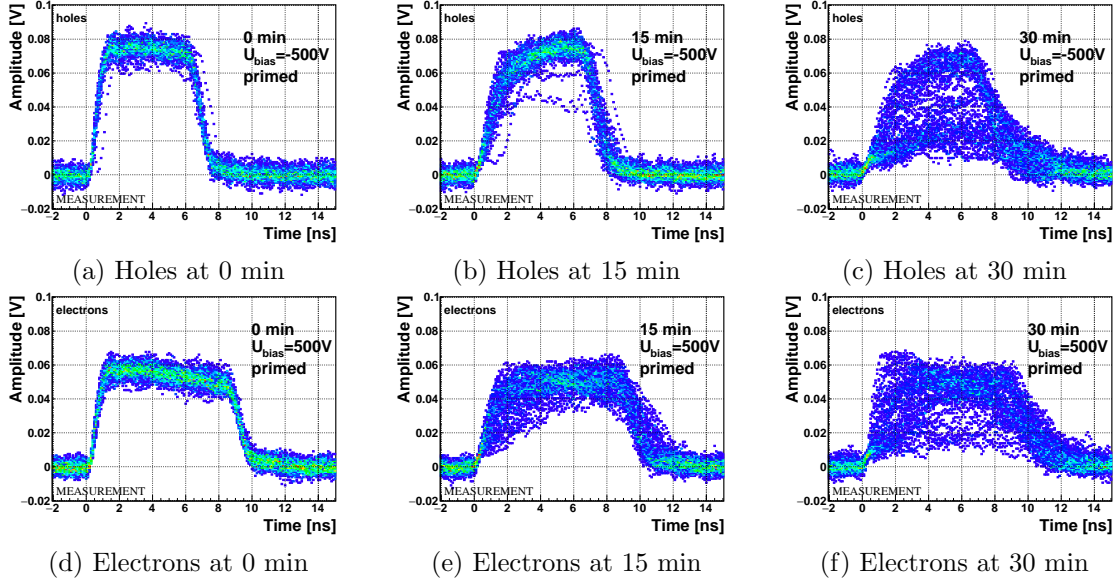


Figure 1.10: This plot shows the signal deterioration of the irradiated and primed S79 with time for both polarities. Every plot contains 60 superimposed pulses.

charge. Since only one charge flavour is drifting through the bulk whereas the other is quickly recombined, this already determines the imbalance in spatial distribution of trapped charges. The built up space charge affects the electric field, making it non-uniform. The non-uniform field in turn affects the drifting carriers, slowing them down or speeding them up, depending on the field gradient. Since the movement of the carriers is the electric current, the field gradient can be observed in the signal. Unfortunately the effects are very convoluted, probably due to the impinging point of the  $\alpha$  particle.

Finally, an effort has put into finding a way for the pulse shapes to return to their initial state. Five methods were tested:

- 453 1. Removing the source and leaving the bias voltage switched on,
- 454 2. Removing the source and switching the bias voltage off,
- 455 3. Priming with  $\gamma$  without bias voltage,
- 456 4. Priming with  $\beta$  with bias voltage switched on and
- 457 5. Priming with  $\beta$  without bias voltage.

458 The diamond sample S79 was first primed using a  $^{90}\text{Sr}$  source for about one hour.  
 459 Then the bias voltage was switched on and an  $^{241}\text{Am}$  source was put on top. The  
 460 pulses produced by the impinging  $\alpha$  particles had a proper rectangular pulse at the  
 461 beginning, but then started changing in an erratic way. After approximately 30 min-  
 462 utes, one of the methods was tested. Then the bias voltage was switched off and the  
 463 sample was primed again to reset its state before starting with the next run.

## 1.4. TEMPERATURE LIMITATIONS

---

At the beginning of every run, 60 reference pulses of the initial pulse were taken and plotted overlapped into a 2D histogram. An average pulse was extracted from this 2D distribution. Then a correlation between the reference pulses and the averaged pulse  $\sigma_{ref}$  was calculated. When a “healing” procedure was started, a set of 60 pulses was taken at irregular points of time to observe the change in the pulse shape. At every data point the correlation with the initial averaged pulse  $\sigma$  was calculated. From the initial correlation  $\sigma_{ref}$  and discrete correlation values  $\sigma$  in time, the shape correlation  $Corr_{shape}$  was calculated and plotted against time on the plot in figure 1.11.

$$Corr_{shape}(t) = \frac{\sigma_{ref}}{\sigma} = \frac{\sum_x \sum_y w_{ref} \cdot (y_{avg} - y_{ref})^2}{\sum_x \sum_y w \cdot (y_{avg} - y)^2} \quad (1.5)$$

It turns out that the methods (3) and (5) improve the shape, method (2) helps slowly, (1) does not show any change with time and (4) at first improves, but then significantly degrades the shape. The effect observed in method (4) has already been described in [?]. The “healing” process therefore depends on the rate of radiation, the bias voltage and the time of exposure. The ionising radiation creates free charges, which quickly recombine close to the place of generation. It is likely that they also release the charges trapped during the measurement, reducing the overall effect of the space charge. The traps get filled with both flavours of carriers, thus they are neutralised. The pulse shape gradually returns to its initial state.

Procedure	Source	Bias voltage	Effectiveness
1	/	ON	no
2	/	/	slow
3	$^{60}\text{Co}$	/	YES
4	$^{90}\text{Sr}$	ON	no
5	$^{90}\text{Sr}$	/	YES

Table 1.2: Effectiveness of healing procedures

To sum up, the shape of the pulses caused by  $\alpha$  radiation changes with time for irradiated samples. The shape of the pulses gets distorted and becomes erratic. Charge collection decreases and its spread increases. This happens even faster for non-primed diamonds. To “heal” the diamond – to bring the pulse shapes back to their initial shape – the sample must be primed using a  $\beta$  or a  $\gamma$  source for several minutes at the bias voltage set to 0 V. Switching to the inverse polarity for a few seconds helps a bit, but in a long run distorts the signal, which cannot get back to its initial shape.

## 1.4 Temperature limitations

A test was carried out to evaluate the effect of temperature changes on the output signal of the diamond sensors. A cryostat filled with liquid helium was used to cool down the sensor during the measurement process. Current signal response to

## 1.4. TEMPERATURE LIMITATIONS

---

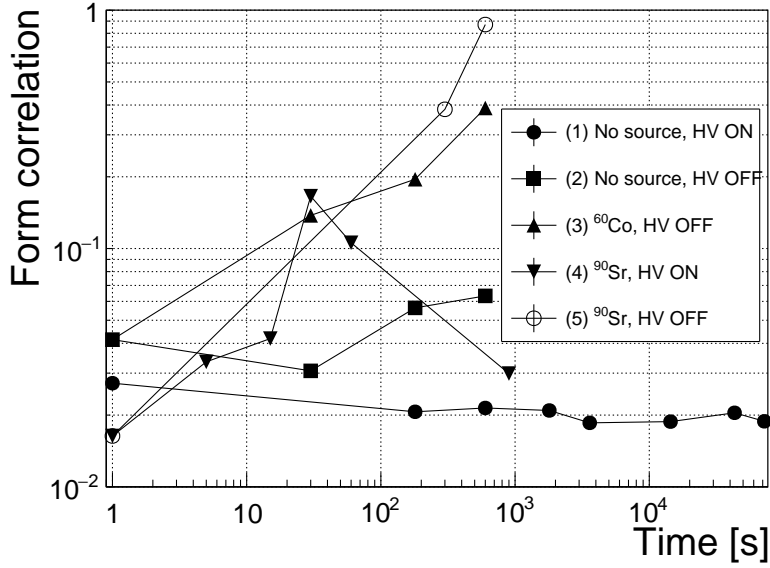


Figure 1.11: Five procedures of the “healing” process for an irradiated diamond that was exposed to  $\alpha$  radiation at bias voltage switched on for at least 30 minutes.

<sup>495</sup>  $\alpha$ -particles was measured at 18 temperature points between 4 K and 295 K (room  
<sup>496</sup> temperature - RT). At every temperature point, a set of 300 pulses was read out at  
<sup>497</sup> various bias voltages. Resulting data showed that the charge collection is stable down  
<sup>498</sup> to 150 K, where it starts decreasing and stabilises again at about one third of the  
<sup>499</sup> initial value at 75 K. This behaviour was first measured and discussed by H. Jansen  
<sup>500</sup> in [?].

<sup>501</sup> The band gap energy in diamond equals to  $E_g = 5.5$  eV while the average energy  
<sup>502</sup> to produce an electron-hole pair is  $E_{e-h} = 13.25$  eV. This means there is excessive en-  
<sup>503</sup> ergy deposited in the diamond bulk. The impinging  $\alpha$ -particle stops within  $\sim 10 \mu\text{m}$   
<sup>504</sup> of the bulk, transferring all its energy to the lattice. A part of this energy, approx-  
<sup>505</sup> imately 40 %, directly ionises the carbon atoms, creating free electron-hole pairs.  
<sup>506</sup> The remaining energy, however, is converted into lattice vibrations (phonons [?]).  
<sup>507</sup> This effectively means that the lattice within the ionisation volume (approximately  
<sup>508</sup>  $\sim 10 \mu\text{m} \times \sim 2 \text{ nm}$  in size) is briefly heated up. The hot plasma then cools down to the  
<sup>509</sup> temperature of the surrounding material by heat dissipation, (i.e. phonon transport).

<sup>510</sup> The positively charged hole and negatively charged electron in the hole attract  
<sup>511</sup> each other via the Coulomb force and may undergo a bonding process during which a  
<sup>512</sup> phonon is emitted. That phonon is referred to as *exciton* [?]. The electron is pushed  
<sup>513</sup> to a exciton energy band, which is 80 mV under the conduction band. At higher  
<sup>514</sup> temperatures, the lattice provides enough energy to excite the electron from the exci-  
<sup>515</sup> ton state back to the valence band (*exciton recombination*). At lower temperatures,  
<sup>516</sup> however, the exciton lifetime increases, which means that it will take a longer time  
<sup>517</sup> for the electrons to get re-excited to the valence band. The re-excitation lifetime at  
<sup>518</sup> room temperature is  $\sim 30$  ps, increasing to  $\sim 150 \mu\text{s}$  at 50 K.

## 1.4. TEMPERATURE LIMITATIONS

---

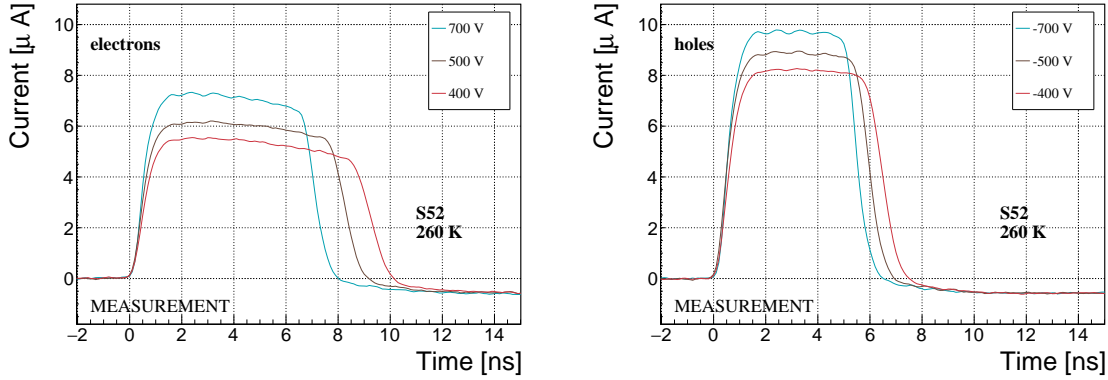


Figure 1.12: Varied bias voltage at a fixed temperature

### 519 1.4.1 Temperature-variant $\alpha$ -TCT before irradiation

520 Three sCVD diamond samples were tested at the range of temperatures using the  
 521  $\alpha$ -TCT technique. At each temperature point, the bias voltage was set to several  
 522 positive and negative values. A set of 300 pulses was recorded at every data point  
 523 and averaged offline. The resulting averaged pulses of sample S37 at the 260 K  
 524 temperature point and a bias voltage of  $\pm 400$  V,  $\pm 500$  V and  $\pm 700$  V are shown in  
 525 figure 1.12. The pulses induced by holes as charge carriers are shorter than those  
 526 induced by electrons, confirming that holes indeed travel faster in diamond. The area  
 527 of the pulse, however, is the same for both polarities, which corresponds to the fact  
 528 that the same amount of charges is drifting in both cases.

529 Figure set 1.13 shows pulses at bias voltage set to  $\pm 500$  V across the range of  
 530 temperatures between 4 K and 295 K – room temperature (RT). Several conclusions  
 531 can be drawn by observing their shape. First, the pulse shapes change with decreasing  
 532 temperature. The pulse time gets shorter, hinting at the faster carrier drift velocity  
 533  $v_{drift}$ . Second, between 150 K and 75 K there is a significant change in shape - the  
 534 time constant of the rising edge increases significantly and the pulse area decreases.  
 535 From 75 K down to 4 K there is no significant observable change. Last, the top of  
 536 the pulse at the S52 is not flat, which means that a portion of the drifting charge is  
 537 lost along its way. This could be due to impurities in the diamond bulk, which act  
 538 as charge traps, or due to the space charge built up in the bulk. A linear pulse top  
 539 hints on the latter. All in all, the pulse shape changes significantly with temperature,  
 540 which is predicted by Jansen's model.

### 541 1.4.2 Temperature-variant $\alpha$ -TCT after irradiation

542 The irradiated S79 and S52 were re-tested in the cryostat. The aim was to see how  
 543 their pulse shapes change with decreasing temperature, in particular the decaying  
 544 top of the pulses (see figure 1.14). The decay time gives information on trapping of  
 545 charge carriers while travelling through the diamond bulk. A variation of the decay  
 546 time constant as a function of temperature might help to reveal the type and depth of

#### 1.4. TEMPERATURE LIMITATIONS

---

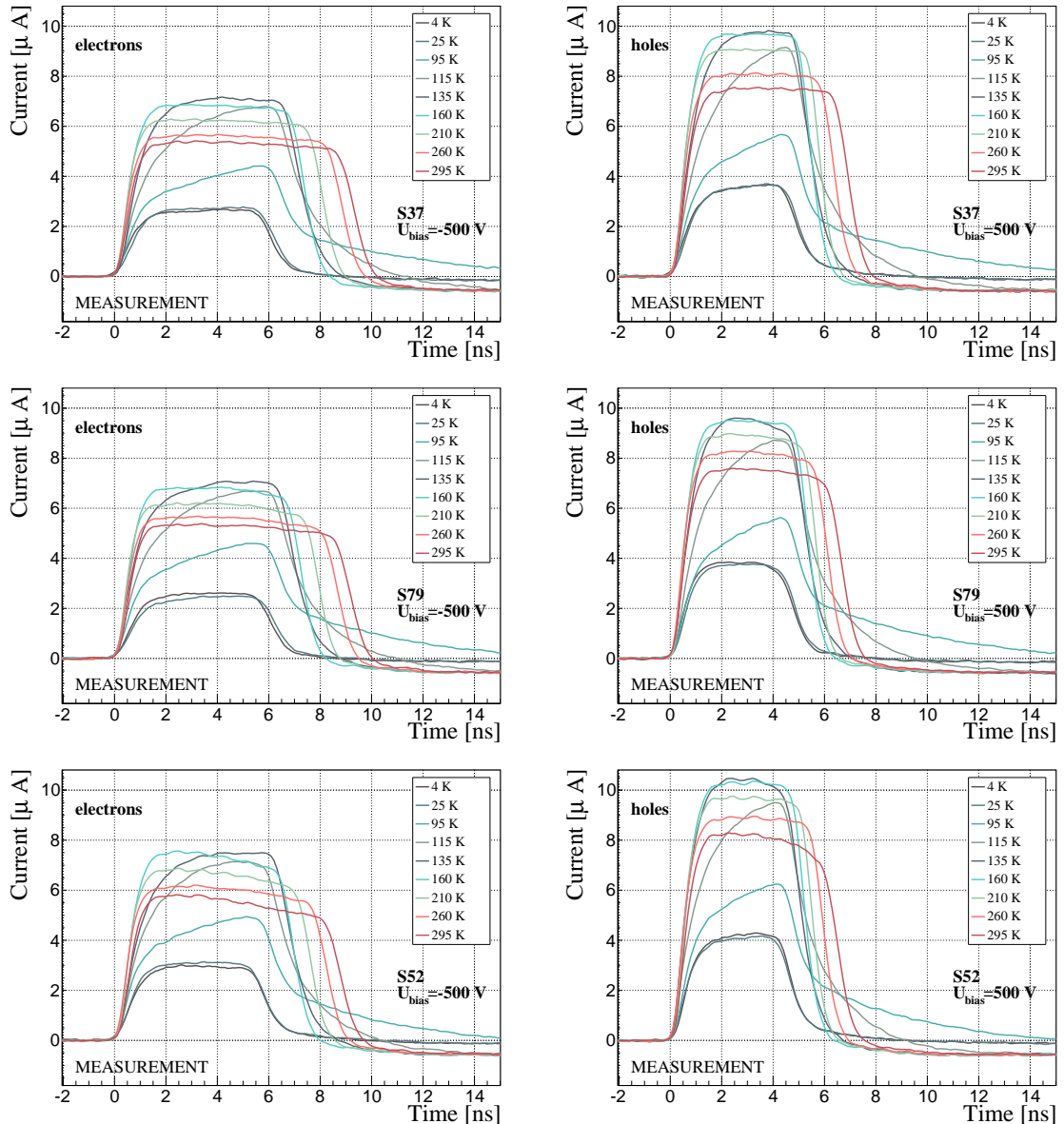


Figure 1.13: Several data points between 4 K and 295 K at a bias voltage of  $\pm 500$  V

## 1.4. TEMPERATURE LIMITATIONS

---

the charge traps. To observe these effects (or lack thereof), a number of requirements had to be met. First, the diamond samples were intentionally not primed prior to the experiment because priming would improve the pulse shapes and the decaying tops. Second, keeping in mind that the pulse shape of irradiated diamonds changes with time, the length of the measurement of an individual data point had to be adequately short. Last, the sequence of the bias voltage settings was important, the reason for which is explained below.

Unfortunately it was not possible to avoid temporal pulse changes. For instance, one measurement point took approximately one minute. After the measurement, the bias voltage polarity was swapped for a few seconds to bring the diamond back into its initial state. But a few seconds with respect to a minute was not enough. Therefore, when the bias voltage was set to the next value, there was still some residual effect of the previous measurement. Similar to the effects of polarisation, this effect was also decreasing the pulse height. This can be observed in figure 1.14, which shows the resulting pulses of S52 for bias voltages of  $\pm 200$  V,  $\pm 300$  V,  $\pm 400$  V and  $\pm 500$  V at 230 K and 260 K. In this case the measurements sequence was: 230K (200 V, 300 V, 400 V, 500 V, -500 V, -400 V, -300 V), 260 K (-200 V, -300 V, -400 V, -500 V, 500 V, 400 V, 300 V). The changes in pulse shapes for holes at 230 K and 260 K cannot be attributed to the temperature change. Instead, the explanation could lie in diamond “*polarisation*”. This means that, when exposed to an electric field with  $\alpha$  measurements ongoing, the diamond builds up the internal electric field of inverse polarity, which effectively reduces the overall electric field. This internal field does not dissipate when the external bias voltage is switched off. It can be said that the diamond is “polarised”. When switching the polarity of the external bias voltage, the internal and external electric field point in the same direction at the beginning, increasing the overall electric field and with it the pulse height. In figure 1.14, this happens when switching from 500 V to -500 V at 120 K. The built up polarisation contributes to the pulse having a sharp rising edge and a high amplitude. This effect decays during the next two voltage points. There would be a handful of ways to avoid this polarisation effect in the data:

1. After every data point invert the bias voltage and leave it to return to a neutral state for the same amount of time,
  2. Make a hysteresis of data points, going from minimum negative to maximum positive bias several times,
  3. Reduce the measurement time at every bias voltage setting.
- Unfortunately, options (1) and (2) are very time consuming and would increase the overall experiment time to over one day. The third option would worsen the resulting averaged pulses. In the end an alternative option was chosen: alternating the starting bias voltage and the sequence at every temperature point. With this option, the highest possible systematic error in analysing the pulse shapes could be attained.

#### 1.4. TEMPERATURE LIMITATIONS

---

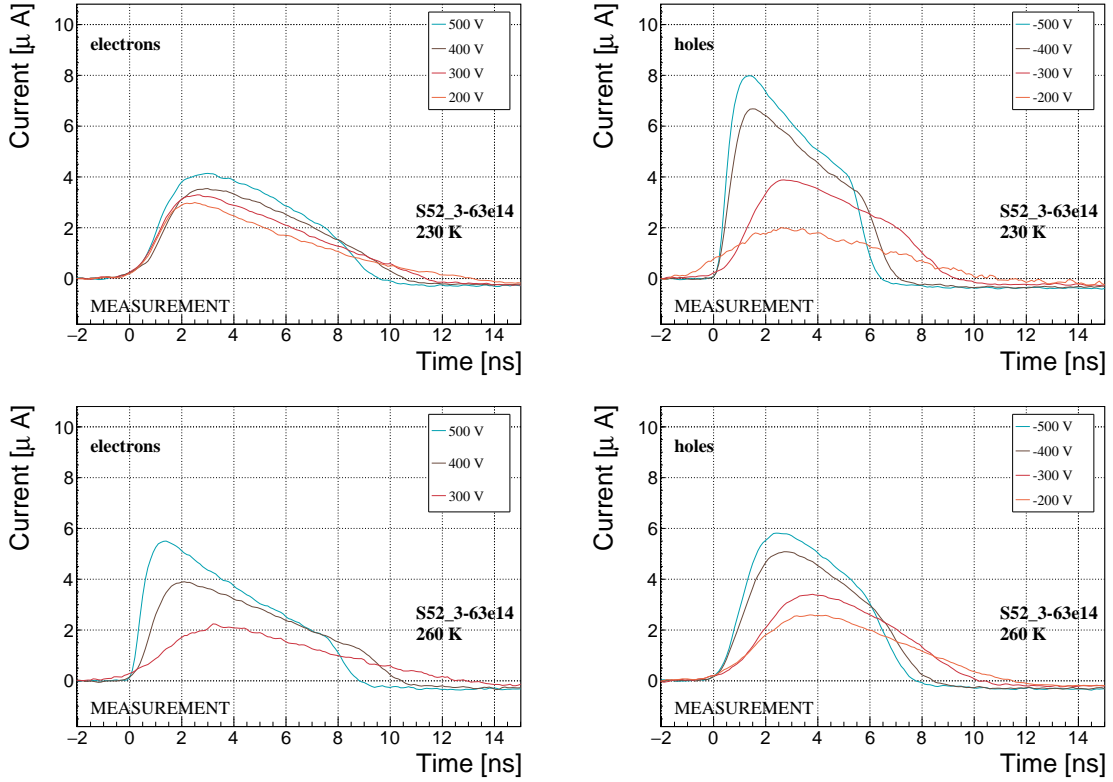


Figure 1.14: Varied bias voltage at a fixed temperature for an irradiated sample

587      Figure 1.15 shows the irradiated S52 and S79 as well as the non-irradiated S37 for  
 588      comparison, all at a bias voltage of  $\pm 500$  V and at several temperature points between  
 589      4 K and RT. It is evident that the irradiation affected the shape of the pulses across  
 590      all temperatures.

591      A decaying exponential function was fitted to the decaying top at pulses at bias  
 592      voltages of  $\pm 400$  V and  $\pm 500$  V across all temperatures excluding the transitional  
 593      range between 75 K and 150 K. There was a spread of fitted values at individual  
 594      temperature points, stemming from the fact that the pulses changed with time due  
 595      to “polarisation”. This counts as a systematic error. Therefore all four fitted values  
 596      were averaged into one value representing the measurement at that temperature point.  
 597      Figure 1.16a shows the fitted decay time constants for the five samples between 4 K  
 598      and 295 K. In principle, the time constants should be infinite for a perfect and non-  
 599      irradiated sample. Here a slightly decreasing top due to space charge was already  
 600      successfully fitted with an exponential function, resulting in a time constant of the  
 601      order of  $200 \text{ s}^{-1}$ . This is also why the spread is enormous. For the irradiated samples,  
 602      the fit becomes increasingly more meaningful. As seen in the plot, the fitted values  
 603      of the irradiated samples are fairly stable across all temperatures. There is a slight  
 604      increase in the decay time constant of the S52 from  $(6 \pm 0.5) \text{ s}^{-1}$  above 150 K to  
 605       $(8.5 \pm 0.9) \text{ s}^{-1}$  below 75 K. On the other hand, this step is not observable in the S79  
 606      data. With only one sample exhibiting this behaviour, the effect is not significant

## 1.4. TEMPERATURE LIMITATIONS

---

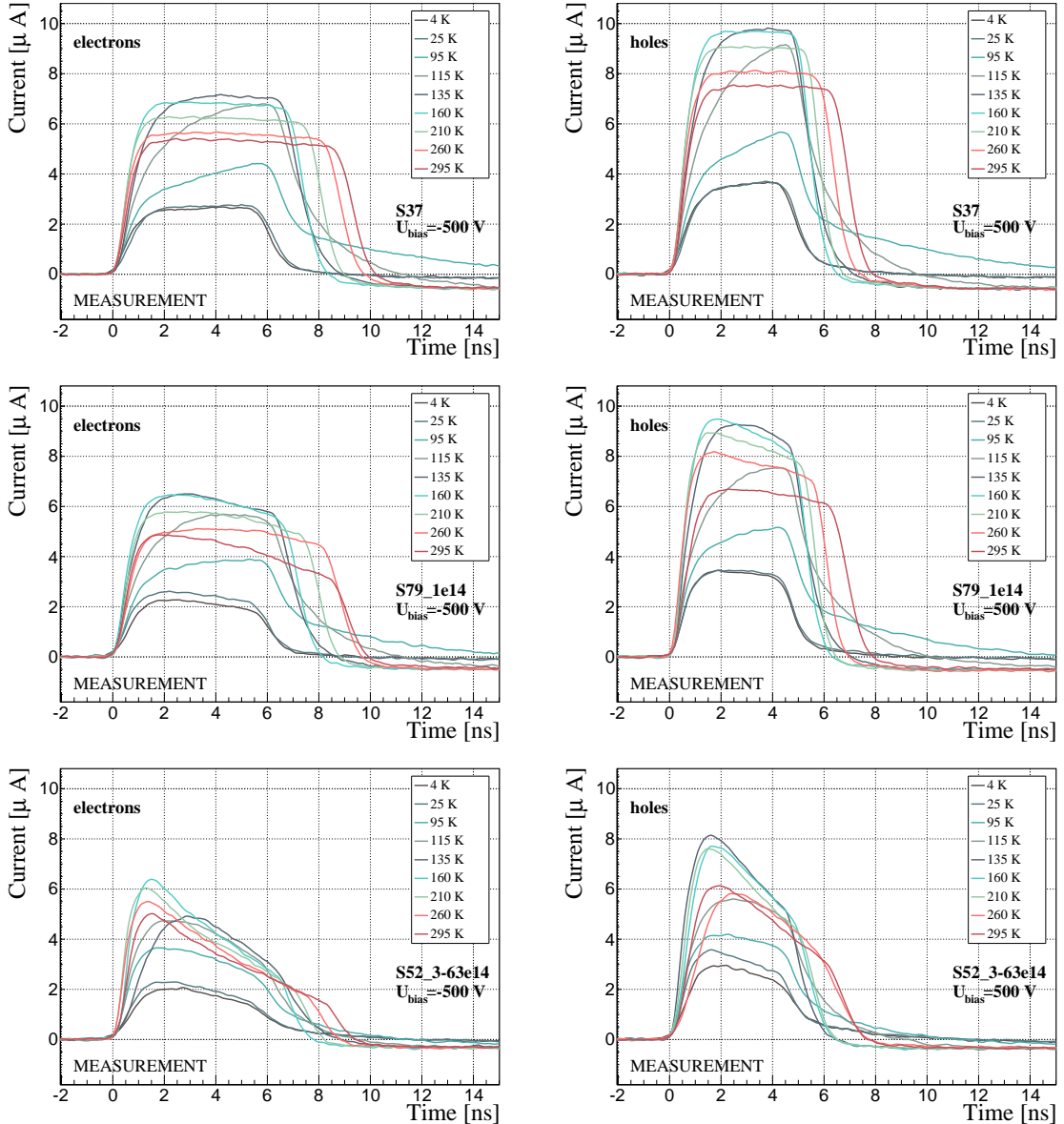


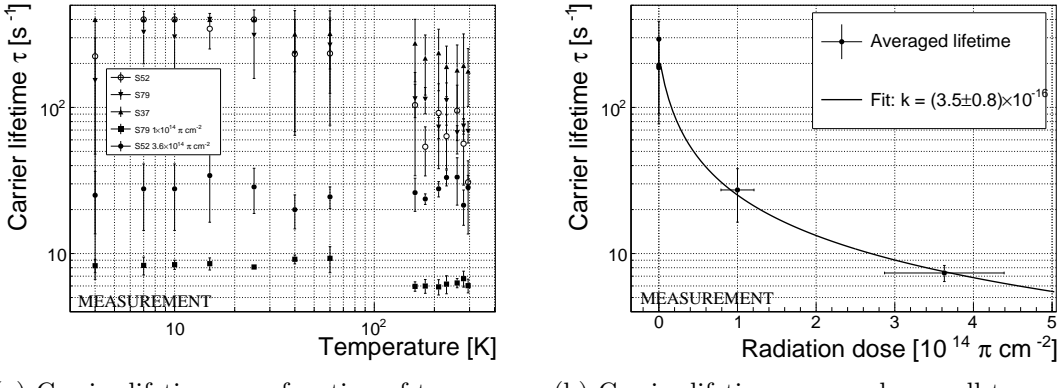
Figure 1.15: After irradiation: several data points between 4 K and 295 K at a bias voltage of  $\pm 500$  V

enough. Judging by the data acquired, the samples would need to be irradiated to doses above  $1 \times 10^{14} \pi \text{ cm}^{-2}$  to quantify this effect in detail. All things considered, this effect will not be regarded as significant for the scope of this thesis. Building on this assumption, the conclusion is that the signal decay time constant for irradiated sCVD diamond is constant across the temperature range between 4 K and 195 K, excluding the transitional range between 75 K and 150 K.

Taking into account the conclusions above, all the values can be averaged into one decay constant. Figure 1.16b shows these values for all samples plotted against received  $\pi$  radiation dose. To estimate the carrier lifetime with respect to the radiation

## 1.5. CONCLUSION

---



(a) Carrier lifetime as a function of temperature

(b) Carrier lifetime averaged over all temperatures as a function of  $\pi$  irradiation dose

Figure 1.16: Charge carrier lifetime decreases with irradiation, but is stable across the range of temperatures between 4 K – 75 K and 150 K – 295 K.

dose received, a similar model was used than that in section 1.5. This model states that the inverse of the carrier lifetime is linearly decreasing with increasing radiation dose:

$$\frac{1}{\tau} = \frac{1}{\tau_0} + \kappa_\tau \cdot \Phi \quad (1.6)$$

$$\tau = \frac{\tau_0}{\kappa_\tau \tau_0 \Phi + 1} \quad (1.7)$$

where  $\tau_0$  is the lifetime for a non-irradiated sample (real lifetime, therefore of the order of 400 s<sup>-1</sup>),  $\tau$  is the lifetime of an irradiated sample,  $\Phi$  is the received radiation dose and  $\kappa_\tau$  the lifetime degradation factor. For these data the fitted factor was equal to  $\kappa_\tau = (3.6 \pm 0.8) \times 10^{-16} \text{ s cm}^2 \pi_{300 \text{ MeV}}^{-1}$ . Using this factor, the steepness of the decay in the pulse shape with respect to radiation dose can be estimated. This can help when designing a system where current pulse shape is an important factor.

## 1.5 Conclusion

This chapter gave an overview of the capabilities and limitations of diamond as a particle detector. Three effects on diamond were studied – noise, radiation and temperature, the focus being on the latter two.

Two sCVD diamond detectors were irradiated with 300 MeV pions. They were tested alongside a non-irradiated sample to observe the changes in the ability to detect  $\alpha$ ,  $\beta$  and  $\gamma$  radiation. Their charge collection efficiency was measured in a test beam facility using . The results were compared to the results from the RD42 collaboration and a DPA model provided by Karlsruhe Institute of Technology, Germany. A radiation damage factor  $k_\lambda = (3.0 \pm 1.0) \times 10^{-18} \mu\text{m}^{-1} \text{ cm}^{-2}$  was obtained for  $\pi_{300 \text{ MeV}}$  particles. The data point did not fully overlap with the data provided by RD42 nor the model. However, the irradiation process and the low number of tested

## 1.5. CONCLUSION

---

638 samples hold a relatively high statistical uncertainty. In addition, there was no di-  
639 amond surface treatment done in between the measurements, as is the case in the  
640 study conducted by RD42. The results obtained in the course of these measurements  
641 will also be fed into the existing pool of data in the RD42 collaboration, increasing the  
642 otherwise rather low number of measurement points of irradiated diamond samples.

643 The next step was to test the long-term capabilities for  $\alpha$  detection. The shape  
644 of the ionisation profile was investigated to determine the behaviour of the charge  
645 carriers in the irradiated diamond. An exponential decay was observed in the pulse,  
646 proving that there are charge traps in the bulk that were created during irradiation.  
647 Then a long-term stability test was carried out. The results show that the irradiated  
648 diamond detectors do not provide a stable and reliable long-term measurement of  
649  $\alpha$  particles. Presumably this is due to a space-charge build-up in the bulk, which  
650 changes the electric field, affecting the charge carriers. A procedure to improve the  
651 pulse shape using  $\beta$  and  $\gamma$  radiation was proposed.

652 Finally, the diamond sensors were cooled down to temperatures between 4 K and  
653 295 K. Their response to  $\alpha$  particles was observed. The results of the non-irradiated  
654 and irradiated samples were compared. The effect of reduction for the number of  
655 drifting charges due to exciton recombination was observed in both sets of data.  
656 The second set had a superimposed effect of charge trapping during the drift, which  
657 was represented by an exponential decay in the signal. The decay time constant  
658 did not change with temperature. Therefore all temperature points for individual  
659 samples were averaged and the decay time constants were plotted against the received  
660 radiation dose. A damage factor equal to  $\kappa_\tau = (3.6 \pm 0.8) \times 10^{-16} \text{ s cm}^2 \pi_{300 \text{ MeV}}^{-1}$  for  
661 non-primed diamonds was defined.